







RESEARCH ARTICLE | DECEMBER 17 2019

## Spin measurements of NV centers coupled to a photonic crystal cavity

T. Jung; J. Görlitz ; B. Kambs ; C. Pauly; N. Raatz; R. Nelz ; E. Neu ; A. M. Edmonds ; M. Markham; F. Mücklich; J. Meijer; C. Becher 



*APL Photonics* 4, 120803 (2019)

<https://doi.org/10.1063/1.5120120>



View  
Online



Export  
Citation

### Articles You May Be Interested In

A low-temperature tunable microcavity featuring high passive stability and microwave integration

*AVS Quantum Sci.* (December 2024)

Multi-color laser excitation of diamond nitrogen vacancy centers embedded in nanophotonic structures

*AIP Advances* (June 2021)

Toward wafer-scale diamond nano- and quantum technologies

*APL Mater.* (January 2019)



APL Photonics

Special Topics Open  
for Submissions

[Learn More](#)

# Spin measurements of NV centers coupled to a photonic crystal cavity

Cite as: APL Photon. 4, 120803 (2019); doi: 10.1063/1.5120120

Submitted: 16 July 2019 • Accepted: 26 November 2019 •

Published Online: 17 December 2019



View Online



Export Citation



CrossMark

T. Jung,<sup>1</sup> J. Görlitz,<sup>1</sup>  B. Kambs,<sup>1</sup>  C. Pauly,<sup>2</sup> N. Raatz,<sup>3</sup> R. Nelz,<sup>1</sup>  E. Neu,<sup>1</sup>  A. M. Edmonds,<sup>4</sup>  M. Markham,<sup>4</sup> F. Mücklich,<sup>2</sup> J. Meijer,<sup>3</sup> and C. Becher<sup>1,a)</sup> 

## AFFILIATIONS

<sup>1</sup>Universität des Saarlandes, Fachrichtung Physik, Campus E2.6, 66123 Saarbrücken, Germany

<sup>2</sup>Universität des Saarlandes, Fachrichtung Materialwissenschaft und Werkstofftechnik, Campus D3.3, 66123 Saarbrücken, Germany

<sup>3</sup>Universität Leipzig, Angewandte Quantensysteme, Linnéstraße 5, 04103 Leipzig, Germany

<sup>4</sup>Element Six Global Innovation Centre, Fermi Avenue, Harwell Oxford, Didcot, Oxfordshire OX11 0QR, United Kingdom

<sup>a)</sup>Electronic mail: [christoph.becher@physik.uni-saarland.de](mailto:christoph.becher@physik.uni-saarland.de)

## ABSTRACT

Nitrogen-vacancy (NV) centers feature outstanding properties such as a spin coherence time of up to 1 s as well as a level structure offering the possibility to initialize, coherently manipulate, and optically read-out the spin degree of freedom of the ground state. However, only about 3% of their photon emission is channeled into the zero phonon line (ZPL), limiting both the rate of indistinguishable single photons and the signal-to-noise ratio (SNR) of coherent spin-photon interfaces. We here report on the enhancement of the SNR of the optical spin read-out achieved by tuning the mode of a two-dimensional photonic crystal (PhC) cavity into resonance with the NV-ZPL. PhC cavities are fabricated by focused ion beam milling in thin reactive ion etched ultrapure single crystal diamond membranes featuring modes with Q-factors of up to 8250 at mode volumes below one cubic wavelength. NV centers are produced in the cavities in a controlled fashion by a high resolution atomic force microscope implantation technique. On cavity resonance, we observe a lifetime shortening from 9.0 ns to 8.0 ns as well as an enhancement of the ZPL emission by almost one order of magnitude. Although on resonance the collection efficiency of ZPL photons and the spin-dependent fluorescence contrast are reduced, the SNR of the optical spin read-out is almost tripled for the cavity-coupled NV centers.

© 2019 Author(s). All article content, except where otherwise noted, is licensed under a Creative Commons Attribution (CC BY) license (<http://creativecommons.org/licenses/by/4.0/>). <https://doi.org/10.1063/1.5120120>

## I. INTRODUCTION

The nitrogen-vacancy (NV) center, a point defect in diamond consisting of a lattice vacancy and an adjacent nitrogen substitution, has attracted a lot of interest during the past years owing to its outstanding optical and spin properties.<sup>1</sup> The triplet ground state exhibits two sublevels attributed to two spin projections  $m_s = 0$  and  $m_s = \pm 1$  of the NV electron spin.<sup>2</sup> In addition to an ultralong spin coherence time of more than 1 s at liquid helium temperatures,<sup>3,4</sup> the NV center features spin-conserving optical transitions.<sup>5</sup> Furthermore, the electron spin may be coherently manipulated by microwave signals<sup>6</sup> and purely optically initialized as well as read-out.<sup>7</sup> Spin initialization and read-out are enabled by a spin-selective

intersystem crossing (ISC) toward the singlet system: the long lifetime in the singlet system facilitates a spin-dependent fluorescence and a preferred decay toward the  $m_s = 0$  ground state,<sup>8,9</sup> allowing for fast spin initialization. Spin polarizations of about 80% at room temperature<sup>10,11</sup> and over 99% at liquid helium temperature<sup>5</sup> may be reached, as well as spin-dependent fluorescence contrasts of up to 30% for an optical spin read-out under nonresonant laser excitation.<sup>12</sup>

Besides the spin-dependent fluorescence contrast, the reliability of an optical spin read-out, designated as the signal-to-noise ratio (SNR), also depends on the detected photon count rate. The SNR for an optical measurement distinguishing between the two possible spin projections  $m_s = 0$  and  $m_s = \pm 1$  of a NV center is

defined as<sup>13</sup>

$$\text{SNR} = \frac{N_0 - N_1}{\sqrt{N_0 + N_1}}. \quad (1)$$

Here,  $N_0$  ( $N_1$ ) is the expectation value for the detected photon count rate when preparing the NV center in the spin projection  $m_s = 0$  ( $m_s = \pm 1$ ). Due to the Poisson-distribution of the photon count rate, we expect that the random variables  $N_0$  and  $N_1$  are also Poisson-distributed;<sup>14</sup> hence, their difference is Skellam-distributed with variance  $\sigma^2 = N_0 + N_1$ .<sup>15</sup> As apparent in Eq. (1), the SNR is mainly determined by the difference  $N_0 - N_1$ . Normalized by  $N_0$ , we obtain the already mentioned spin-dependent fluorescence contrast  $C = (N_0 - N_1)/N_0$ . With this measure, we get the relation

$$\text{SNR} = \sqrt{N_0} \cdot \frac{C}{\sqrt{2 - C}}. \quad (2)$$

As visible from Eq. (2), a large SNR of optical spin read-out requires both a large collected photon rate and a large contrast of spin-dependent fluorescence.<sup>16</sup> In view of applications, a sufficiently large SNR improves the use of NV centers as quantum sensors for temperature,<sup>17</sup> pressure,<sup>18</sup> as well as magnetic fields on the nanoscale.<sup>19–22</sup> Furthermore, it facilitates the NV based verification of fundamental principles of quantum mechanics, e.g., as demonstrated by a loop-hole free Bell test.<sup>23</sup> Furthermore, a high enough SNR in combination with the long spin coherence time enables the coupling of NV centers to nearby nuclear spins used as quantum bits<sup>24–27</sup> or as building blocks of quantum repeaters.<sup>28,29</sup> In particular, for an aspired scaling of quantum systems toward quantum networks,<sup>30</sup> a speed-up of the entanglement generation is a central requirement and hence a preferably large SNR desirable.

The photon detection rate is usually limited by a nonperfect photon collection. Consequently, several approaches to enhance the collection efficiency have been followed by modifying the directivity of emission such as using an optimal crystal orientation,<sup>31</sup> fabricating solid immersion lenses around NV centers,<sup>5,32</sup> or incorporating NV centers in nanopillars,<sup>33,34</sup> nanowires,<sup>35</sup> waveguides,<sup>36,37</sup> or metalenses.<sup>38</sup> Furthermore, the collection efficiency can be modified by coupling NV centers to whispering gallery,<sup>36,39</sup> photonic crystal (PhC),<sup>40–44</sup> or fiber-based cavities<sup>45,46</sup> as well as to plasmonic structures.<sup>47,48</sup> In addition, by such a coupling, the local density of states at the emitter's position and hence its spontaneous emission rate may be enhanced or, correspondingly, the spontaneous emission lifetime reduced by the Purcell-factor  $F$ .<sup>49</sup> In addition, the coupling of NV centers to a cavity has the advantage that more than the usual 3% of the photons are emitted into the zero phonon line (ZPL). Hence, entanglement generation by interference of ZPL photons at a beam splitter<sup>23,50–52</sup> may be further sped up by coupling to a cavity featuring a mode in resonance with the NV-ZPL. However, a modification of the population dynamics, such as Purcell enhancement of emission, also influences the spin-dependent fluorescence contrast  $C$ . Bogdanov *et al.* showed that for NV ensembles in nanodiamonds, the contrast decreases when reducing the emitter's lifetime by coupling to plasmonic islands.<sup>48</sup> Furthermore, Babinec *et al.* in a theoretical study found that the spin read-out SNR achieves a maximum value for Purcell-factors on the order of 1.<sup>53</sup>

In this article, we report on the SNR enhancement achieved by coupling NV centers to a two-dimensional PhC cavity. Successful

coupling of NV centers to low mode volume, tunable cavities was recently also demonstrated employing thin diamond membranes embedded into Fabry-Pérot microcavities.<sup>45</sup> While this approach includes a lower level of fabrication complexity compared to PhC cavities, the diamond membranes need to feature a very smooth surface (roughness  $\lesssim 1$  nm rms) to avoid intracavity scattering losses.<sup>54</sup> The design of open Fabry-Pérot microcavities advantageously provides both spectral and spatial tunability to selected emitters but at the same time, gives rise to sensitivity to vibrations in the experimental setup. Typically, vibrations have to be kept below  $\approx 0.1$  nm rms to couple a large fraction of the NV ZPL emission to the cavity mode.<sup>54</sup> On the other hand, PhC in diamond are monolithic, on-chip cavity systems. Due to the monolithic design, spectral tuning requires elaborate modifications of the dielectric boundary conditions, e.g., by changing the diamond membrane thickness by oxidation or gas adsorption (see Sec. III). At the same time, however, cavity resonances are not prone to vibrations, as demonstrated by the results of this work where we did not find any differences in cavity Q factors for operation at ambient conditions or cryogenic temperatures in a closed-cycle cryostat. In addition, we did not observe any drifts, instabilities, or degradation of cavity resonances over the time span of a few weeks operating time in the cryostat.

We here report on a fabrication process starting from ultra-pure single crystal diamond membranes bonded on a sacrificial silicon substrate. After thinning by reactive ion etching (RIE), two-dimensional PhC cavities are fabricated by focused ion beam (FIB) milling at thoroughly characterized and carefully selected membrane positions.<sup>55</sup> NV centers are subsequently incorporated into the PhC cavities by a high resolution atomic force microscope (AFM) implantation technique.<sup>56</sup> A FIB-milled hole in the AFM-tip serves as an aperture, which enables the accurate implantation of nitrogen into the cavities. We activate the NV centers by extensive post processing, i.e., annealing and cleaning procedures. We further report on the deterministic spectral tuning of a cavity mode into resonance with the NV-ZPL using thermal oxidation of diamond as well as condensation of residual gas in the cryostat. We finally experimentally measure and theoretically simulate the modification of spin-dependent fluorescence contrast  $C$  and SNR on resonance.

## II. CAVITY FABRICATION AND NV INCORPORATION

### A. Sample system with FIB-milled cavities

The Purcell-factor  $F$ , quantifying the lifetime reduction achieved by the emitter-cavity-coupling, is directly proportional to the ratio of quality factor  $Q$  and modal volume  $V$  of a PhC cavity mode. The  $Q$ -factor is strongly dependent on the precision of fabrication and deviations from the design parameters. In order to produce PhC cavities with modes featuring a high  $Q$ -factor and a spectral position close to the NV-ZPL, diamond membranes with a precise thickness are required. However, due to polishing wedges as well as local deviations in the etching rate during RIE-thinning, the thickness typically varies over the diamond film by several hundred nanometers.<sup>55</sup> Therefore, the thinned membranes need to be characterized carefully in order to select suitable spots for the subsequent cavity production. The challenge in FIB milling of the PhC array is

the fabrication of regularly hole patterns with vertical hole sidewalls. Conical shapes with typically observed inclination angles of as large as  $9^\circ$  may degrade the  $Q$ -factor by one order of magnitude.<sup>55,57</sup> The fabrication process and characterization methods are described in detail in our previous publication.<sup>55</sup>

The sample system is depicted in Fig. 1(a). As starting material, we use  $30\ \mu\text{m}$  thick, chemical vapor deposition (CVD) grown, (001)-oriented, ultrapure, single crystal diamond membranes (electronic grade quality, ElementSix) with a nitrogen concentration below 5 ppb. We note that other diamond orientations, especially (111), would orient the NV center's dipoles more optimal with respect to the PhC cavity mode. However, (001)-oriented diamond still provides the highest material quality and highest availability. We note that, in principle, anisotropic RIE recipes are transferable to (111)-diamond, e.g., as demonstrated via fabrication of (111)-oriented nanopillars.<sup>58</sup>

At first, the diamond film is etched by RIE in an  $\text{Ar}/\text{O}_2$ -plasma to remove  $5\ \mu\text{m}$  of the surface material as its quality is degraded due to the polishing process.<sup>59</sup> After acid-cleaning, the remaining  $20\ \mu\text{m}$  thick diamond film is, mediated by a spin-coated  $50\ \text{nm}$  thick layer of hydrogen silsesquioxane (HSQ XR-1541-002, DowCorning), bonded to a silicon substrate containing pre-fabricated windows. Curing the sample system at  $600^\circ\text{C}$  renders the bond persistent during the postprocessing and cleaning procedure required after FIB milling as well as for removing damages in the diamond crystal lattice after nitrogen implantation (see Sec. II B). Furthermore, the stable bond allows measurements at liquid helium temperatures. The final membrane thickness of a few hundred nanometers is finally reached by further RIE thinning from topside.

The membranes are subsequently characterized by laser-scanning microscopy, cross section measurements, and quantitative dispersive X-ray spectroscopy. The combination of these methods maps the thickness of the diamond films as well as the surface structure with high resolution, and we select defect-free spots featuring a suitable thickness for the fabrication of PhC cavities.

M0-cavities generated by a shift of two adjacent holes [Fig. 1(b)] are fabricated by FIB milling. We chose PhC's hole radii of  $R = 68\ \text{nm}$  and the lattice constant of  $a = 250\ \text{nm}$  such that the cavity modes match the NV-ZPL position at  $637\ \text{nm}$ . In addition, the M0-cavity is optimized by slight changes in position and/or radii of holes close to the point-defect.<sup>60</sup> The simulated  $Q$ -factor of the cavity mode is  $320\ 000$  at a mode volume of  $0.35\ (\lambda/n)^3$ .

In order to obtain a conical hole shape below  $4^\circ$  with sharp and well-defined hole edges at optimized positions, we employ several optimizations. First, we use overmilling and drift control programs during the FIB process. This is accompanied with chamber pressures below  $5 \times 10^{-6}$  mbar and a temperature stabilization of the ion-column. Eventually, a metal protection layer prior to the FIB milling is employed. After an extended postprocessing, consisting of annealing steps in vacuum at  $1000^\circ\text{C}$  and acid-cleaning, the fabricated cavities are analyzed in a home-built confocal setup. The PhC cavities feature modes with  $Q$ -factors up to 8250, as depicted in Fig. 1(c). Hence, the  $Q$ -factors obtained here are on par with  $Q$ -factors of two-dimensional PhC cavities with small modal volumes (around one cubic wavelength) at the wavelength of NV centers, as currently observed from RIE fabrication methods.<sup>40,44,61</sup>

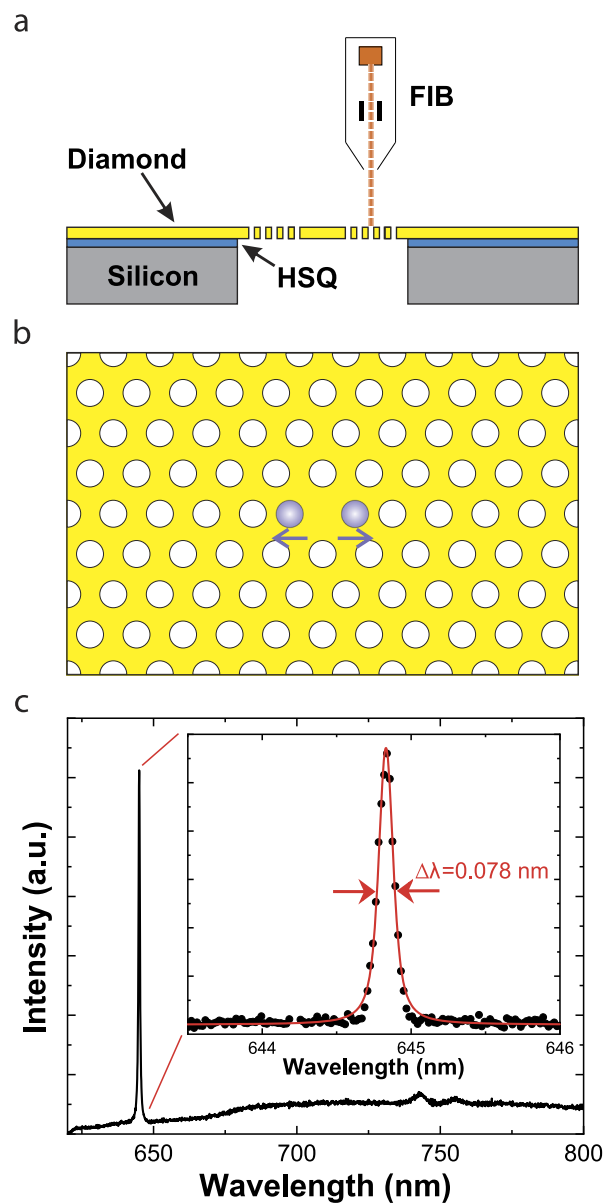


**FIG. 1.** (a) A silicon substrate structured with windows on the scale of  $150 \times 150\ \mu\text{m}^2$  is spin-coated with a  $50\ \text{nm}$  thick HSQ layer. A CVD-grown, ultrapure, single crystal diamond film is positioned on the HSQ layer generating an air suspended diamond membrane. After RIE thinning from the topside, the diamond has a final thickness of a few hundred nanometers. PhC cavities are produced by FIB milling at preselected defect-free spots with a suitable thickness. (b) Scheme of a M0-cavity generated by a slight shift of two adjacent holes. (c) Photoluminescence (PL) spectroscopy of a M0-cavity at room-temperature. The cavity mode at  $644.8\ \text{nm}$  features a FWHM of  $0.078\ \text{nm}$ , corresponding to a  $Q$ -factor of 8250. The spectra were taken with an integration time of  $30\ \text{s}$  under nonresonant laser excitation at  $532\ \text{nm}$  and a laser power of  $1\ \text{mW}$ .

## B. NV incorporation by AFM implantation

This section summarizes how we generate NV centers located at the field maximum of the PhC via nitrogen ion implantation.

In the past few years, several high resolution implantation techniques were developed, most of them masking the sample surface by spin-coated photoresist films,<sup>62,63</sup> Mica layers,<sup>64</sup> transferred silicon hard masks,<sup>65</sup> as well as structured AFM-tips.<sup>56</sup> Each of the methods features small holes as apertures. Also, a maskless FIB-implanter was realized.<sup>66</sup> The last two techniques have the outstanding advantage that the implantation spot can be positioned relative to previously produced nanostructures with an accuracy at the nanoscale. Whereas the lateral resolution of a nitrogen FIB implantation is about 100 nm at a typical acceleration voltage of 30 kV, nitrogen may be implanted through an AFM-tip with a lateral resolution of up to 20 nm at a typical implantation energy of 5 keV.<sup>67</sup> As precise positioning is crucial for efficient cavity coupling, we here use the AFM-tip technique.

The home built AFM-setup combines a conventional low-energy ion source for generation and acceleration of nitrogen ions with an AFM-unit. A small hole is FIB-milled close to the apex of the pyramidal AFM-tip which is positioned over the implantation spot [Fig. 2(a)]. To align the AFM-tip relative to the sample, AFM-scans are performed prior to every implantation [Fig. 2(b)]. The lateral implantation resolution with regard to the diameter of the

AFM-aperture of 70 nm, the alignment accuracy of the tip to the sample of about 1 nm, and the ion straggle in diamond of 3 nm at the chosen implantation energy of 5 keV yields a total accuracy of 74 nm. Note that small straggling effects of ions at the edges of the 70 nm aperture are not included in the analysis above and are under present investigation. The expected implantation depth of the nitrogen ions in (001)-oriented diamond samples is 13 nm on average,<sup>68</sup> and the expected yield is about 0.8%.<sup>69</sup> The implantation dose aiming at one NV center per cavity is calculated to  $2.7 \times 10^{12}$  ions/cm<sup>2</sup>. As the generation of NV centers is a statistical process, the final implantation doses were varied between half and triple of the calculated value.

After implantation, an extensive postprocessing is required in order to restore a good diamond crystal quality and to activate NV centers. To this end, the samples are first annealed in vacuum ( $p \leq 10^{-6}$  mbar) at 900 °C for 10 h. Subsequently, oxidation of the samples at 450 °C for 3 h in air atmosphere and acid cleaning (5 h in a tri-acid mixture of perchloric, sulfuric, and nitric acid) removes graphitic residuals from the surface and provides an oxygen termination. Hence, the possibility to obtain negatively charged NV centers within the PhC cavity is enhanced.<sup>70</sup>

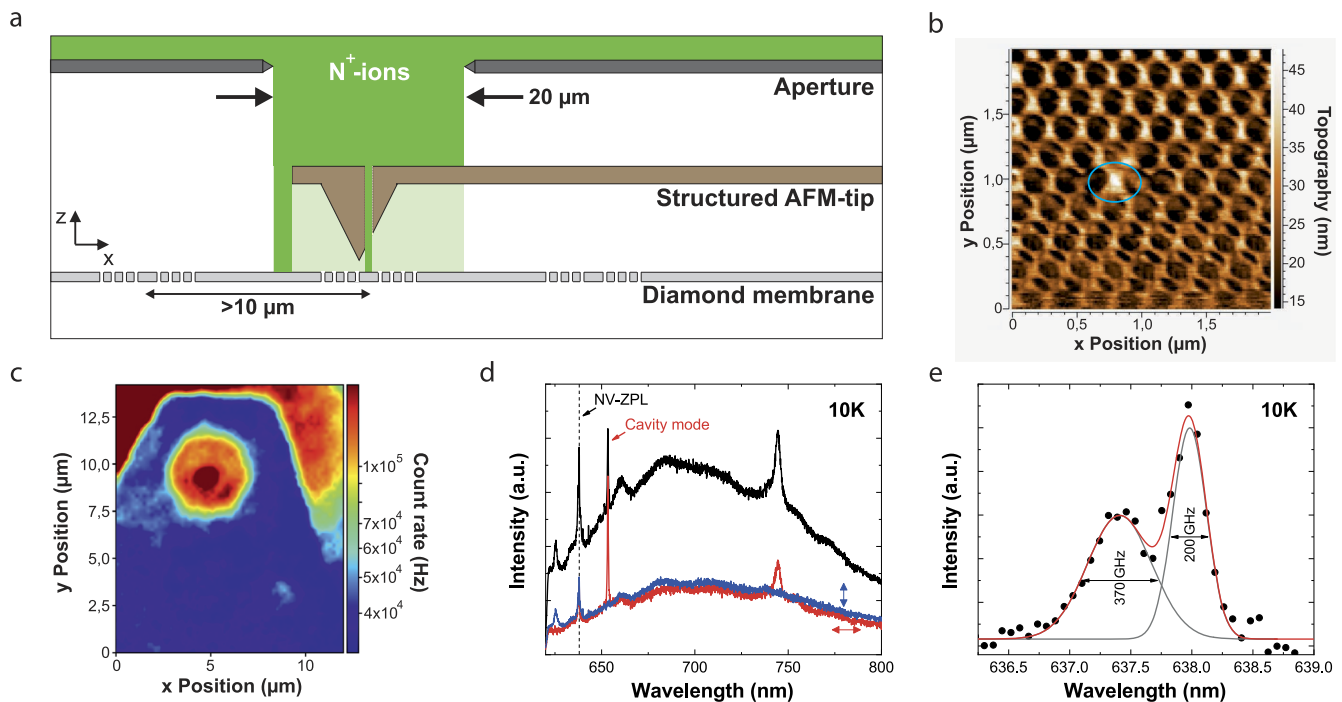


**FIG. 2.** AFM implantation: (a) The prefocused nitrogen ion beam is at first narrowed down to a diameter of 20  $\mu\text{m}$  by an aperture and subsequently focused by electrostatic lenses (not sketched) on the backside of the AFM-tip. The final beam diameter of 70 nm is defined by a FIB-milled hole drilled through the AFM-tip. After the alignment of the AFM-tip relative to the sample, nitrogen ions are implanted into the cavities. The surrounding nanostructure is protected by the AFM-cantilever against unintended ion bombardment. (b) Topography of a M0-cavity recorded by an AFM-scan (noncontact mode). The cavity area is clearly visible (marked blue). (c) Spatially resolved PL image of a M0-cavity with a resolution of 100 nm. The count rate is detected in a filter window between 650 nm and 750 nm on the NV sideband and scaled logarithmically. [(d) and (e)] PL spectra of the very same M0-cavity at a temperature of 10 K. (d) The cavity mode has a Q-factor of 2060. In addition, a spectral line around 638 nm is observable, attributed to the NV-ZPL. The blue and the red curve are spectra with a horizontal/vertical polarization filter in the detection path. (e) By zooming into the spectrum around 638 nm, two peaks get clearly visible, which can be fitted by Gaussian lines (gray). The spectra were taken with an integration time of 120 s. The laser excitation in (c)–(e) was carried out at a wavelength of 532 nm and a laser power of 500  $\mu\text{W}$ .

In Fig. 2(c), a typical spatially resolved photoluminescence (PL) image after postprocessing is shown. Generated NV centers are localized in the PhC cavities as well as outside the area masked by the AFM-cantilever. This observation is in agreement with the results of additionally performed optically detected magnetic resonance (ODMR) measurements, which reveal a dip at frequencies around 2.87 GHz, characteristic for NV centers,<sup>7</sup> inside the cavities, and no hints of NV centers within the surrounding PhC arrays. The cavities were further examined with PL spectroscopy at low temperatures. In Figs. 2(d) and 2(e), PL spectra of the M0-cavity with the lowest applied implantation dose are shown. Besides, the cavity mode spectral lines around 638 nm are visible featuring Gaussian shapes with half widths (FWHM) of 200 GHz and 370 GHz, respectively. We performed photon correlation ( $g^2$ ) measurements to estimate the number of generated NV centers. As the  $g^2$  results did not show a dip but Poissonian photon statistics, we have to assume that a few NV centers were created inside the cavity volume. The deviation from the expected implantation yield might be explained by a large number of defects in the material as a consequence of the PhC fabrication process, providing a high density of vacancies for NV center creation. In addition, the emission lines might be shifted by local strain and strongly broadened by spectral diffusion due to nearby charges.<sup>71,72</sup> For applications requiring single NV centers such as spin-photon interfaces, a mean number of one NV center per cavity could be achieved by reducing the implantation dose. Quantum sensing applications (e.g., detecting magnetic fields), however, profit from the  $\sqrt{N}$  scaling of the sensitivity with the number  $N$  of NV centers.

### III. RESONANCE TUNING

In the past few years, several techniques have been developed for the deterministic tuning of cavity modes into resonance with the ZPL of color centers. A well-established but irreversible method is the oxidation of diamond in an air or oxygen atmosphere.<sup>41,73</sup> At temperatures above 450 °C, the diamond surface starts to oxidize and the thickness of the diamond membrane decreases with an accompanying enlargement of the hole diameters. Both effects lead to a spectral blue shift of the cavity modes: Finite Difference Time Domain (FDTD) simulations predict a blue shift of 12 nm for our M0-cavity if 5 nm of diamond are removed from the surface. On the other hand, cavity modes have been successfully redshifted by condensing inert gases like xenon or nitrogen on the sample's surface,<sup>41,74,75</sup> thereby increasing the sample thickness and reducing the hole radii. In contrast to the oxidation technique, a tuning by gas adsorption is a reversible process where heating the sample enables the residual-free removal of the condensed layers.<sup>75</sup>

In the following, we focus on the M0-cavity implanted with the lowest implantation dose of  $1.35 \times 10^{12}$  ions/cm<sup>2</sup>, featuring a cavity mode with a Q-factor of 2060 [spectra in Figs. 2(d) and 2(e)]. At first, the oxidation technique described above, using a temperature of 525 °C, is applied to tune the cavity mode to shorter wavelengths. After tuning and acid-cleaning, the resulting mode position is 634 nm. In a second step, the residual gas present in the sample chamber of the cryostat (Attodry 2100, Attocube) is adsorbed to the sample, allowing a redshift of the cavity mode under continuous optical control: we observed that during PL measurements

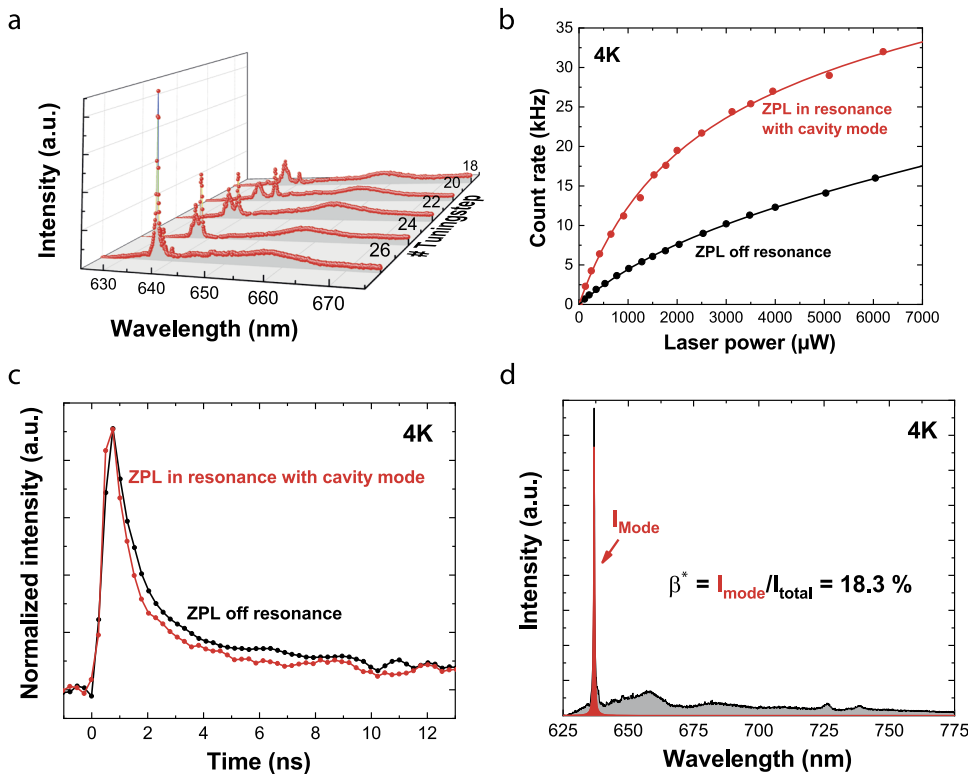


**FIG. 3.** Tuning the mode of a M0-cavity into resonance with the NV-ZPL at 637.4 nm. (a) PL spectra after different tuning steps. (b) Comparison of a resonant (red) to an off-resonant (black) saturation measurement and (c) comparison of a resonant (red) to an off-resonant (black) lifetime measurement. The off-resonant measurements were performed with the cavity mode tuned to 634 nm. The ZPL photons were detected in a filter window around 638 nm featuring a spectral width of 2.5 nm. (d) Estimation of the emission fraction into the cavity mode from the PL spectrum. The ratio of the area below the Lorentzian line (red) and the area below the entire curve (gray + red) yields the corresponding intensity ratio.

at room-temperature and a pressure of  $10^{-4}$  mbar, cavity modes show a red shift under continuous laser excitation at 532 nm. Furthermore, only the modes of a cavity directly irradiated with laser light are affected and the observed shift rates scale with the power. All these observations may be explained as follows: as the vacuum pump is attached at the top side of the cryostat, pumping leads to an efficient removal of lightweight molecules, whereas heavy gas molecules, e.g., hydrocarbons, partly remain in the sample chamber. Based on the observations, we assume a light-assisted adsorption of residual gas molecules onto the sample's surface.<sup>75,76</sup> Under illumination with 1.5 mW of laser light at 532 nm, we observe a shift rate of the cavity modes of approximately 1.8 nm/h. The  $Q$ -factor remains almost unchanged with  $Q = 2021$  after tuning. Importantly, after further pumping and cooling to liquid helium temperatures, no further mode shifts are observable under laser illumination (over the duration of the experiment of several weeks) within the resolution limit of our spectrometer ( $<0.1$  nm). We point out that the described tuning by gas adsorption is a reversible process. Heating the sample to 400 °C in air atmosphere resets the sample to the initial state before the gas adsorption.

The PL spectra depicted in Fig. 3(a) show a strong enhancement of the ZPL intensity by tuning the cavity mode on resonance. We further observe an enhancement of the saturation count rate filtered in a 2.5 nm wide window by a factor of 2.8 from 13.6 kHz to 37.5 kHz [Fig. 3(b)]. Furthermore, the emitter's lifetime decreases from 9.0 ns at a spectral mode position of 634 nm to 8.0 ns in resonance with the NV-ZPL. The recorded lifetime traces [Fig. 3(c)] feature a double exponential decay. The second time constant on the order of 1 ns may be attributed to fast decaying fluorescence in the diamond membrane (background). Moreover, PL spectra allow for the estimation of the fraction of emission into the cavity mode as well as the resulting Purcell-factor. The deduced spontaneous emission coupling factor on resonance is  $\beta^* = I_{\text{mode}}/I_{\text{total}} = 18.3\%$  [Fig. 3(d)]. As the incorporated NV centers feature an off-resonant Debye-Waller factor of 2.1%, we conclude that the emission fraction into the ZPL is strongly enhanced due to the cavity coupling.

The  $\beta^*$ -factor finally enables us to calculate the total Purcell-factor to be  $1 + F^* = 1.224$ . For comparison with theoretical expectations, we modeled the total Purcell-factor  $1 + F^*$  on resonance by using a phonon assisted cavity coupling model presented in Ref. 77. With the  $Q$ -factor and modal volume  $V$  of the cavity mode as well as the measured linewidths of the ZPL and the sideband transitions of the NV centers, a Purcell-factor of  $1 + F^* = 4.9$  is predicted. The experimentally determined value of  $1 + F^* = 1.224$  is reduced due to a nonperfect lateral positioning of the implanted NV centers relative to the mode field, a shallow implantation depth, as well as a nonperfect dipole orientation in the used (001)-oriented diamond samples. The model further correctly predicts the experimentally observed lifetime reduction.

To analyze the NV-ZPL in detail, a photoluminescence excitation (PLE) spectrum was recorded for wavelengths between 636.2 nm and 638.5 nm. In the spectrum depicted in Fig. 4, it is notable that only one of the previously detected two emission lines [see Fig. 2(e)] remains. In the PLE spectrum, this line at 637.4 nm has a half width of 360 GHz, in good agreement with the value of 370 GHz deduced from the PL spectra. The absence of the second line is most likely due to the removal of shallow implanted NV centers during the extended tuning steps by oxidation.

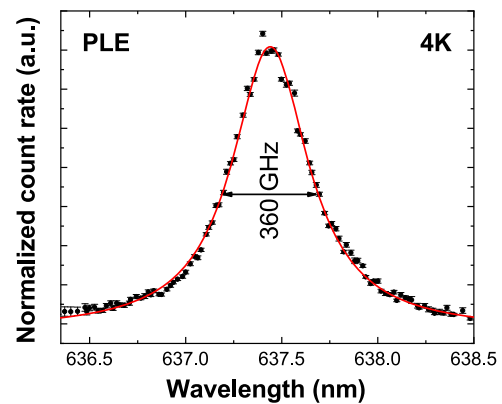


FIG. 4. PLE spectrum of the NV-ZPL in the M0-cavity. The count rates detected on the NV sideband in a filter window ranging from 650 nm to 750 nm are normalized to the laser power of a tunable diode laser and fitted by a Lorentzian line (red).

#### IV. SNR ENHANCEMENT

To estimate the SNR enhancement due to the emitter-cavity-coupling, we at first have to consider the change in the photon count rate  $N_0$ . For this, we have to take into account the shortening of the emitter's lifetime as well as the change in collection efficiency. Furthermore, for the SNR, the change in spin-dependent fluorescence contrast  $C$  has to be considered. To this end, a reliable methodology is required to compare the contrast before and after tuning the cavity mode in resonance with the NV-ZPL.

##### A. Light extraction from a PhC cavity

We simulate the emission of the cavity-coupled NV centers using finite element software (FDTD solutions, Lumerical) by modeling the emission of an electric dipole point source positioned in the mode field maximum. The simulated photonic nanostructure features the same number of holes as the produced M0-cavity where the holes have a conical shape with an inclination angle of  $4^\circ$  (see Sec. II). We calculate the emission fractions in the two half-spaces above and below the PhC as well as the collection efficiency for a microscope objective (NA = 0.8) positioned vertically above the diamond membrane. Each simulation is performed for an  $E_z$  dipole oriented vertically to the diamond film as well as for the in-plane dipoles  $E_x$  and  $E_y$ . These dipoles are oriented such that the cavity mode is fed by the  $E_y$  dipole, whereas the  $E_x$  dipole has orthogonal polarization. The orthogonality of the dipoles also allows us to calculate the emission for arbitrary dipole orientations as discussed below.

As an example, we show in Fig. 5(a) a simulation for the  $E_y$  dipole. We find that the collection efficiency drops to 3.4% at the resonance wavelength of the cavity mode, whereas for other wavelengths within the photonic bandgap, collection efficiencies around 25% are achieved. This minimum arises from a modified directional characteristic of the emitted light. Two factors play a role here: first, the fraction of photons emitted in the top half-space decreases from over 50% in the bandgap to below 12% at cavity resonance [Fig. 5(a)]. Second, a smaller part of the photons emitted in the top

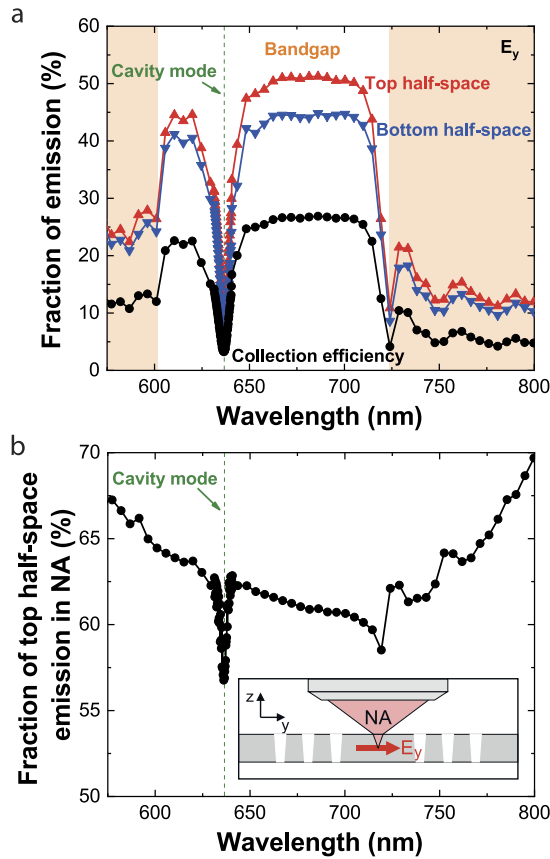


**FIG. 5.** Simulation of the light emission from a MO-cavity for a dipole oriented in the  $y$ -direction ( $E_y$ ). (a) Collection efficiency (black), fraction of the emitted photons into the top half-space (red) and the bottom half-space (blue). Sectors outside the photonic bandgap of the underlying PhC array are marked orange. (b) Fraction of the top half-space light emitted in farfield angles  $\leq 51.13^\circ$ , which may be collected by a microscope objective with NA = 0.8.

half-space (below 57% instead of over 62%) can be collected within the NA at the resonance wavelength of the mode [Fig. 5(b)].

The NV emission dipoles are oriented in the (111)-plane of the diamond lattice. For the small NV ensemble in our experiment, we average over all possible dipole orientations within the (111)-plane. As the used diamond material features a (001)-orientation, the  $\langle 111 \rangle$ -axis exhibits an angle of  $35.3^\circ$  to the  $xy$ -plane (membrane plane). The projection of the averaged NV dipoles onto the  $x$ -axis or  $y$ -axis amounts to 24% and 52% onto the  $z$ -axis. To calculate the resulting collection efficiency for our NV ensemble, also the Purcell-factors for the three dipole orientations have to be considered. The emission directivity of photons emitted into the cavity mode is only determined by the mode emission directivity. Further, the emission directivity of off-resonant photons is defined by the photonic nanostructure. Considering this, we first calculated the spontaneous emission rates  $\tilde{\gamma}_i$  of the projections of the averaged NV dipoles onto the  $x$ -,  $y$ -, and  $z$ -axis considering the corresponding Purcell-factors  $F_i$  as follows:

$$\tilde{\gamma}_i = \gamma \cdot F_i \cdot k_i \quad (3)$$

with the free-space spontaneous emission rate  $\gamma$ ,  $k_i = 0.24$  for  $i = x, y$  and  $k_i = 0.52$  for  $i = z$ . Subsequently, the fraction of emission produced by the averaged NV dipole projected to the  $x$ -,  $y$ -, or  $z$ -axis may be calculated by normalizing the spontaneous emission rates  $\tilde{\gamma}_i$  to the sum over all these rates. To finally calculate the collection efficiency at the given dipole orientation, the simulated collection efficiencies for a dipole oriented in  $x$ -,  $y$ -, or  $z$ -direction are weighted with the respective fraction of emission and the resulting values summed up.

For the optical read-out of the NV electron spin, we can distinguish between two fundamental cases. In the first case only ZPL photons are considered. This is, for instance, the case if indistinguishable photons are required. On the other hand, for projective spin read-out, generally all the emitted photons are used, e.g., if NV centers are used as magnetic field sensors on the nanoscale.<sup>19–22</sup> The simulations predict a collection efficiency of 3.9% for the off-resonant mode position at 634.0 nm, which is slightly reduced to 3.4% in resonance with the NV-ZPL. Hence, if for the spin read-out only ZPL photons are used, the collection efficiency drops by a factor of 0.87. If in the second case, all emitted photons are used for the spin read-out, the collection efficiency drops only by a factor of 0.97. The reduction in the second case is smaller as only a fraction of the emitted photons is affected by the dominant decrease in collection efficiency at the resonance wavelength of the cavity mode.

### B. Fluorescence contrast measurements

We apply a protocol composed of three succeeding measurements for the reliable and reproducible determination of the time-resolved, spin-dependent fluorescence contrast of the cavity-coupled NV centers. For the considered off-resonant coupling (PhC cavity mode at 634 nm) at first, an ODMR-measurement under continuous laser and microwave excitation is performed. An external magnetic field of 2 mT is applied to split the two ground state sublevels  $m_s = -1$  and  $m_s = +1$ . Hence, in the ODMR-spectrum in Fig. 6(f), two dips are visible belonging to the resonance frequencies of the ground state transitions from  $m_s = 0$  to  $m_s = -1$  and  $m_s = +1$ , respectively. In the following, we only focus on the transition to the  $m_s = +1$  sub-level featuring a resonance frequency of  $\nu_{+1} = 2.917$  GHz. For all presented measurements, the optical excitation of the NV centers is carried out in the PL saturation regime.

To determine the population inversion time, a Rabi measurement on the transition  $m_s = 0$  to  $m_s = +1$  is performed [Fig. 6(a)]. From the observed damped Rabi oscillations, a  $\pi$ -time of 550 ns and a spin coherence time of  $T_2^* = 1.5 \mu\text{s}$  are deduced. As the Rabi frequency  $\Omega_R < 1/T_2^*$ , the measured coherence time should not be influenced by decoupling effects (typically requiring  $\Omega_R \gg 1/T_2^*$ ) but might be reduced by technical noise such that the given value for  $T_2^*$  is a conservative estimate. Furthermore, the value of  $T_2^*$  is in accordance with typical spin coherence times observed for shallow NV centers in nanophotonic structures based on single crystal diamond<sup>78</sup> and the spin coherence time  $T_2^* = 2.1 \mu\text{s}$  of a small ensemble of NV centers implanted into the same sample but outside the cavity region. This indicates that our PhC fabrication process does not adversely influence the NV spin coherence properties.

In Fig. 6(b), we present the time-resolved, spin-dependent fluorescence. Here, after spin initialization, a resonant microwave  $\pi$ -pulse is applied, resulting in a preparation of the NV centers in



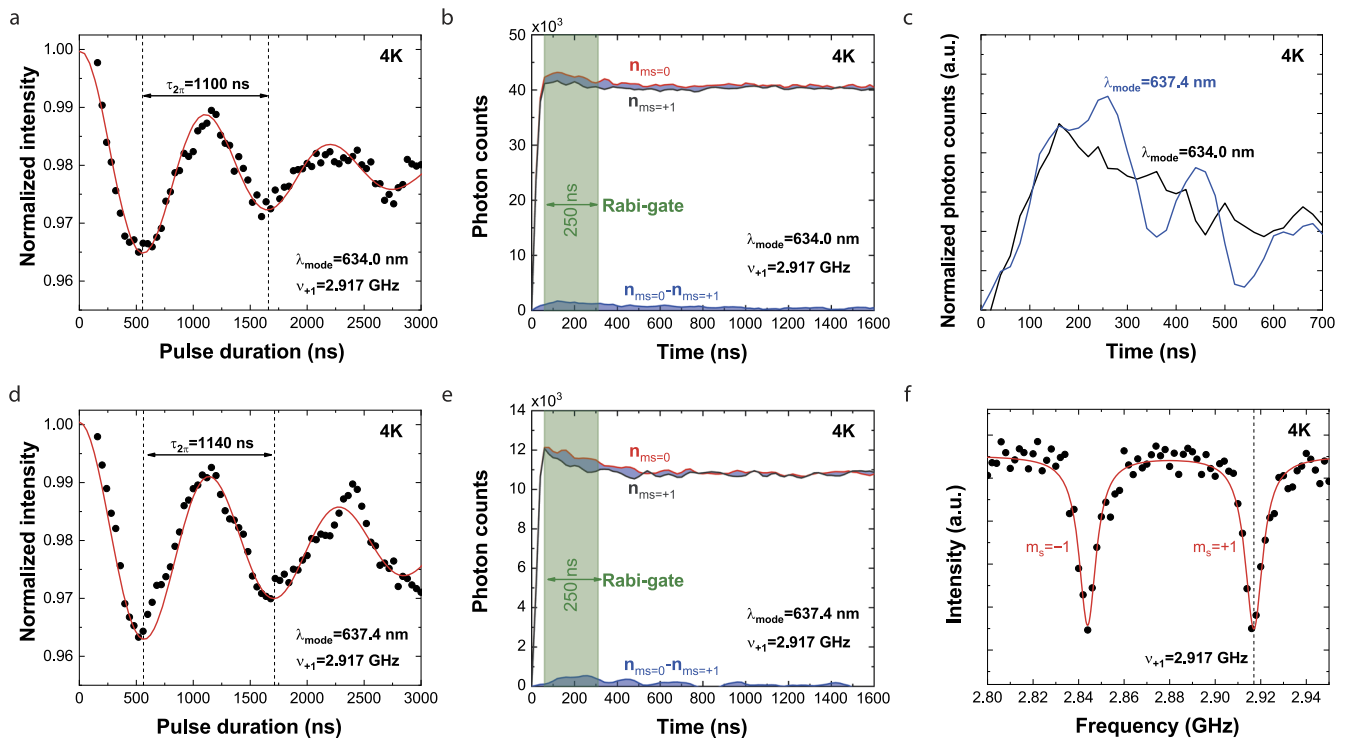


**FIG. 6.** Fluorescence measurements at liquid helium temperature for the cavity-coupled NV centers off [(a) and (b)] and on [(d) and (e)] resonance. [(a) and (d)] Rabi measurements. The NV ensemble is initialized in  $m_s = 0$  using a  $2 \mu\text{s}$  laser pulse at  $532 \text{ nm}$  followed by a resonant microwave pulse of variable length. During a read-out laser pulse, the fluorescence is detected in a  $250 \text{ ns}$  wide photon detection gate. The data are fitted by exponentially damped sinusoids (red). [(b) and (e)] Time-resolved fluorescence for the NV centers prepared in the  $m_s = 0$  state (red) and  $m_s = +1$  state (black) as well as the resulting time-resolved fluorescence contrasts (blue). The fluorescence contrasts plotted in (c) are normalized to the corresponding photon counts in the steady state. (f) Continuous wave ODMR measurement at an external magnetic field of  $2 \text{ mT}$ . The excitation is carried out by an off-resonant laser at  $532 \text{ nm}$  in the PL saturation regime. The photons are detected on the NV sideband between  $650 \text{ nm}$  and  $750 \text{ nm}$ . The detected photon count rates are background corrected.

the  $m_s = +1$  state. During the spin read-out, a  $50 \text{ ns}$  wide photon detection gate is temporally shifted. For each gate position, the measurement is repeated for a NV preparation in the  $m_s = 0$  state and the difference of the two fluorescence curves is calculated, yielding the time-resolved fluorescence contrast. As expected, the fluorescence curves at first rise for both spin states, whereas the count rate for the  $m_s = 0$  state (*bright state*) is generally higher as for the  $m_s = +1$  state (*dark state*) with a maximum contrast of  $C = 4.2\%$ . With progressing laser excitation time, both fluorescence curves converge toward a joint value, indicating an equilibrium, spin-mixed state. Whereas the fluorescence contrast measured on single NV centers under zero magnetic field can reach values of  $20\%$ <sup>79</sup> to  $30\%$ ,<sup>12</sup> for NV ensembles in a magnetic field, contrasts of only a few percent are expected.<sup>80</sup> Possible reasons are lattice and surface defects introduced by FIB milling, impairing charge state stability and spin coherence of the shallow implanted emitters.<sup>80,81</sup> Furthermore, a strain gradient may locally alter the ground state splitting. Hence, different emitters of the considered small NV ensemble may feature slightly different resonance frequencies.

Subsequently, the cavity mode is tuned into resonance with the NV-ZPL (see Sec. III). As for the tuning process, the sample has to be dismounted from the cryostat, a repositioning of the microwave

antenna, an air suspended gold wire loop mounted on a positioner, is required after remounting the sample. To establish comparable experimental conditions, we position the antenna in such a way that a  $\pi$ -time of  $570 \text{ ns}$  is reached [Fig. 6(d)], in good agreement with the  $\pi$ -time of  $550 \text{ ns}$  [Fig. 6(a)] for the NV-ZPL off resonance with the cavity mode. We follow the same protocol as in the off-resonant case to measure Rabi oscillations [Fig. 6(d)] as well as fluorescence curves [Fig. 6(e)] on resonance. When comparing the resulting time-resolved fluorescence contrast on- and off-resonance [Fig. 6(c)], we find a small reduction in contrast of  $1.5\%$  on resonance [integrated over the entire time interval in Fig. 6(c)].

### C. Rate equation model

To analyze the measured spin-dependent fluorescence contrast, we setup a rate equation model following Wolf *et al.*<sup>14</sup> In this model, a NV center is adopted as a five level system [Fig. 7(a)], consisting of the two ground states  $m_s = 0$  and  $m_s = \pm 1$ , respectively, the corresponding excited states and a long-living singlet state. For the modeling, we assume that the excitation rates out of the two ground states are identical for the nonresonant laser excitation.<sup>82</sup> Furthermore, it is assumed that the emission rates from the excited to the

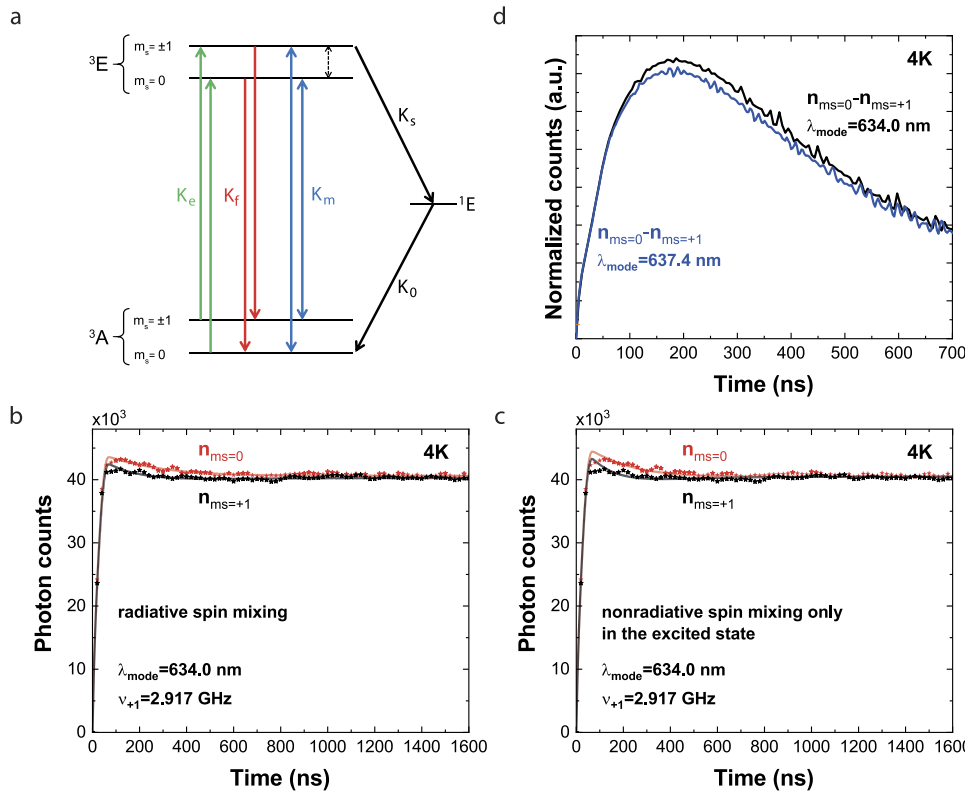


**FIG. 7.** Rate equation model. (a) NV center modeled as a five level system. The radiative triplet transitions [both spin-conserving (green, red) and spin-mixing (blue)] are illustrated as colored and the ISC transitions are illustrated as black arrows. The dashed arrow indicates a scenario where nonradiative spin-mixing happens in the excited state. [(b) and (c)] Measured time-resolved, spin-dependent fluorescence after preparing the NV centers in the  $m_s = 0$  state (red dots) and  $m_s = \pm 1$  state (black dots) for the NV centers off resonance with the cavity mode. The modeled curves (red and black lines) were adapted for the rates  $K_e = K_f = 111$  MHz under the assumption of a radiative spin-mixing (b) and a nonradiative spin-mixing in the excited state (c), respectively. (d) Simulated fluorescence contrast of NV centers off (black curve) and on (blue curve) resonance with the cavity mode under the assumption of a spin-mixing due to ISC and by radiative transitions in the triplet system.

ground states of the triplet system are spin independent.<sup>83</sup> In addition, the transition rate from the excited  $m_s = 0$  state to the singlet state is neglected as this rate is four orders of magnitude smaller than the corresponding transition rate for the  $m_s = \pm 1$  state.<sup>8,83,84</sup> As a further assumption, the transition rate from the singlet state to the  $m_s = \pm 1$  ground state is neglected because the rate to the  $m_s = 0$  ground state is about six times larger.<sup>8,9</sup> By reason of these assumptions, a spin-mixing, leading to a statistical mixture of  $m_s = 0$  and  $m_s = \pm 1$  states due to the spin-selective intersystem crossing, is already included in the model. Such a spin-mixing was both theoretically predicted<sup>9,14,48</sup> and experimentally confirmed.<sup>8</sup>

If, however, the only spin-mixing process was due to ISC, the modeled population would end up in the  $m_s = 0$  state for sufficient long-lasting laser excitation and the modeled fluorescence would thus be maximized. Instead, the spin-dependent fluorescence curves in our experiment [Figs. 6(b) and 6(e)] as well as for other NV centers (see, e.g., Refs. 11 and 13) show a convergence toward a steady state. Therefore, a further spin-mixing has to be included in the model. Wolf *et al.* propose on the one hand a radiative spin-mixing between the excited and ground states of the triplet system and on the other hand a purely nonradiative spin-mixing between the excited states.<sup>14</sup> As can be seen in Figs. 7(b) and 7(c), respectively, the measured data may be fitted well under the assumption of a radiative spin-mixing and, in particular, better than under the assumption of a nonradiative spin-mixing in the excited state. However, Kalb *et al.* demonstrated that a radiative spin-mixing occurs only with a probability of well below 1% and hence should not be

the dominant spin-mixing mechanism in our experiments.<sup>8</sup> Instead, the reason for the additionally observed spin-mixing mechanism is that in our experiments, we apply an external magnetic field to split the ground states of the NV centers (see Sec. IV B). As the diamond sample features a (001)-surface and the magnetic field an orientation vertical to the diamond's surface, the magnetic field exhibits an angle of  $54.7^\circ$  to the magnetic dipole axis of the NV centers. As now both ground and excited states consist of a superposition of bare, zero-field spin states, optical transitions with spin flips become allowed resulting in an effective radiative spin mixing.<sup>85</sup> Furthermore, the rates of ISC transitions are modified. Therefore, in summary, the data are fitted appropriately under the assumption of a spin-mixing due to ISC and by radiative transitions in the triplet system.

In the following, we assume for simplicity that the spin-mixing induced by the off-axis magnetic field is the same for excitation and emission. With this, the following rate equations are setup, determining the internal dynamics of a NV center,

$$\begin{aligned}
 \dot{B}_{G,0} &= -(K_e + 2K_m)B_{G,0} + K_f B_{E,0} + K_m B_{E,1} + K_0 B_S, \\
 \dot{B}_{G,1} &= -(K_e + K_m)B_{G,1} + K_f B_{E,1} + 2K_m B_{E,0}, \\
 \dot{B}_{E,0} &= K_e B_{G,0} - (K_f + 2K_m)B_{E,0} + K_m B_{G,1}, \\
 \dot{B}_{E,1} &= K_e B_{G,1} - (K_f + K_s + K_m)B_{E,1} + 2K_m B_{G,0}, \\
 \dot{B}_S &= K_s B_{E,1} - K_0 B_S.
 \end{aligned}
 \tag{4}$$

$B_{G,0}$  and  $B_{G,1}$  are the populations of the ground states  $m_s = 0$  and  $m_s = \pm 1$ ,  $B_{E,0}$  and  $B_{E,1}$  are the populations of the corresponding excited

states, and  $B_S$  is the population of the singlet state.  $K_e$  and  $K_f$  are the spin-preserving excitation and emission rates,  $K_s$  is the transition rate from the excited  $m_s = \pm 1$ -state to the singlet state,  $K_0$  is the transition rate from the singlet state to the  $m_s = 0$  ground state, and  $K_m$  is the rate of the radiative spin-mixing induced by the off-axis magnetic field. As the measurements are performed in the PL saturation regime, the relation  $K_e = K_f$  holds in the following.

According to the measured off-resonant lifetime value of 9.0 ns, a decay rate of  $K_f = 111$  MHz is set in the model. With the parameters  $K_e$  and  $K_f$  fixed, the rate equations are solved and the simulated time-resolved fluorescence is fitted to the measured curves by varying the free parameters  $K_0$ ,  $K_s$ , and  $K_m$  [Fig. 7(b)]. From this fit, a spin-mixing rate of  $K_m = 1.35$  MHz, a transition rate to the singlet state of  $K_s = 1.79$  MHz, and a transition rate to the  $m_s = 0$  ground state of  $K_0 = 5.80$  MHz are determined.

These rates together with the model [Eq. (4)] allow us to theoretically predict the time-resolved, spin-dependent fluorescence contrast for on- and off-resonant coupling [see Fig. 7(d)]. The theoretically predicted fluorescence contrast on resonance is slightly lower than for the off-resonant case. This is expected as the emission rate  $K_f$  scales with the Purcell-factor and the probability for spin-mixing is the larger the more fluorescence cycles occur per time unit. Depending on the position as well as the size of the temporal read-out window, a reduction in the fluorescence contrast by tuning the mode into resonance with the NV-ZPL of up to 5% is theoretically predicted. For a realistic read-out photon gate of 250 ns, as, for instance, typically used for the acquisition of Rabi measurements, the fluorescence contrast would be reduced by 4.1%.

Such a reduction is conformable with the experimental results (see Sec. IV B).

#### D. Implications for the SNR

We now discuss the modification of the spin measurement SNR induced by the modified photon collection and modified spin-dependent fluorescence contrast due to the cavity coupling. With Eq. (1) as well as the appropriate assumption of small contrasts, we arrive at

$$\zeta = \frac{\text{SNR}^*}{\text{SNR}} \approx \sqrt{\frac{N_0^*}{N_0}} \cdot \frac{C^*}{C}, \quad (5)$$

where variables with (without) a star indicate the on- (off-) resonant case. Based on the presented measurements as well as the theoretical modeling, we assume in the following, a reduction in the spin-dependent fluorescence contrast by 4.1%, i.e.,  $C^*/C = 0.959$ . Due to the lifetime reduction, the number of emitted photons is increased by a factor of 1.13, when the mode is tuned into resonance with the NV-ZPL. If we, in a first scenario, consider only ZPL photons for spin read-out, the collection efficiency is reduced by a factor of 0.87 (see Sec. IV A). Furthermore, the fraction of photons emitted into the ZPL is modified from 2.1% off resonance to 18.3% on resonance [see Fig. 3(d)], resulting in an enhancement factor of 8.7. The total estimated enhancement of the collected photons by applying a narrow-band photon detection around the ZPL is hence  $N_0^*/N_0 = 1.13 \times 0.87 \times 8.7 = 8.5$ . Consequently, following Eq. (5), the SNR is enhanced by a factor of  $\zeta = 2.8$ . As a result, the SNR is almost tripled by tuning the mode into resonance

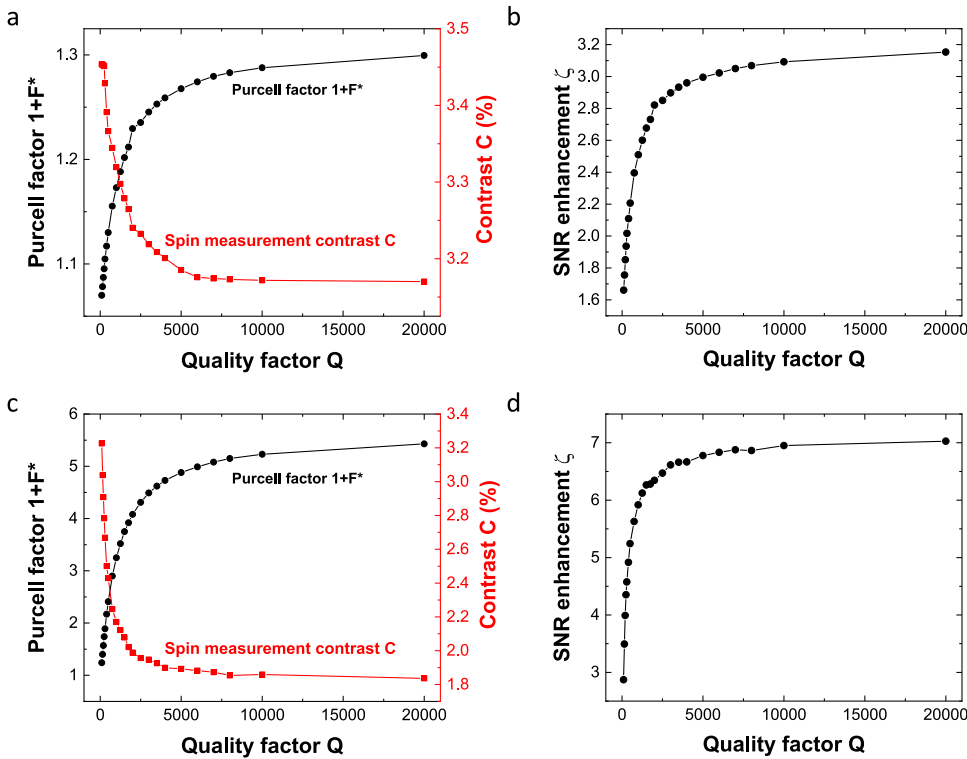


**FIG. 8.** Purcell factor  $1 + F^*$  and spin measurement contrast  $C$  [(a) and (c)] as well as the resulting SNR enhancement  $\zeta$  [(b) and (d)] as a function of the cavity Q factor. The values were calculated with the here presented rate equation model. For the upper graphs [(a) and (b)], realistic coupling parameters reached by our cavity coupling were applied, taking into account a nonperfect lateral positioning of the implanted NV centers, a shallow implantation depth as well as a non-perfect dipole orientation. For the lower graphs [(c) and (d)], an ideal cavity coupling was assumed.

with the NV-ZPL. Figure 8(a) shows a simulation of Purcell factor  $1 + F^*$  and spin measurement contrast  $C$  as a function of the cavity quality factor  $Q$ , assuming realistic parameters as determined above. We find that the Purcell factor saturates at values  $Q \approx 5000$ , whereas the spin measurement contrast  $C$  monotonically decreases due to the enhanced spin mixing and also saturates for similar  $Q$  factors. Under these realistic coupling conditions, the maximum achievable SNR enhancement [Fig. 8(b)] is  $\zeta = 3.2$ , demonstrating that our system was operating close to the optimum cavity  $Q$  factor.

If we, in a second scenario, consider the collection of all photons for the spin read-out, we cannot benefit from the higher emission fraction into the ZPL anymore, but the number of emitted photons is still enhanced by a factor of 1.13 due to the lifetime shortening on resonance. The collection efficiency is here reduced by a factor of 0.97 (see Sec. IV A). Altogether, the number of detected photons by applying a broad-band photon detection is enhanced by a factor of  $N_0^*/N_0 = 1.13 \times 0.97 = 1.10$ , resulting in a very small SNR enhancement of about 0.5%. In summary, the cavity coupling of NV centers as demonstrated here leads to a spin read-out SNR enhancement of up to a factor of  $\approx 3$ . This factor is within the same order of magnitude as the SNR enhancement achieved by other methods for improving the photon collection efficiency.<sup>5,13,31</sup>

## V. CONCLUSIONS

In summary, we reported on the SNR enhancement of the optical spin read-out achieved by tuning the mode of a two-dimensional PhC cavity into resonance with the NV-ZPL. To achieve this, ultra-pure (001)-oriented CVD-grown diamond films were used as starting material for the RIE fabrication of thin, air-suspended membranes. An extended characterization allowed us to select defect-free spots featuring a suitable thickness for the subsequent fabrication of PhC cavities by FIB milling. The analyzed cavity modes showed  $Q$ -factors of up to 8250 at mode volumes of less than one cubic wavelength. The application of a high-resolution implantation technique using a pierced AFM-tip allowed the subsequent generation of NV centers in the cavities. The combination of two spectral tuning methods, an oxidation technique for the blue shift and a gas adsorption technique for the red shift, facilitated the reliable and precise tuning of a cavity mode. For the considered cavity-coupled NV centers, the SNR was almost tripled. A theoretical model, taking into account the measured shortening of the emitter's lifetime, the measured and theoretically predicted change in fluorescence contrast as well as the simulated modification of the collection efficiency reproduces the experimental findings very well.

Whereas the reported SNR enhancement is on par with simpler methods for photon collection enhancement,<sup>5,13,31</sup> it could be still increased by a further optimized cavity coupling: a (111)-oriented diamond sample with an optimal dipole orientation may lead to a fourfold enhancement of the total Purcell-factor. For an optimal implantation depth in the center of the diamond film, instead of the shallow implantation, the Purcell-factor may be further increased by a factor of 3.2. In total, for an optimal cavity coupling, our theoretical model predicts a SNR enhancement by a factor of up to 7. A possible method to reach this ideal coupling scenario is a change of the fabrication order such that at first, NV centers are implanted into the diamond film and subsequently a PhC

cavity is fabricated around. This scenario is displayed in Figs. 8(c) and 8(d), showing a simulation of Purcell factor  $1 + F^*$  and spin measurement contrast  $C$  as a function of the cavity quality factor  $Q$  for ideal emitter-cavity coupling. In comparison to the realistic case, both Purcell factor and contrast saturate at even smaller values of  $Q$ . This again demonstrates that large SNR enhancements do not require very large  $Q$  factors.

A change of the fabrication order would allow a maskless implantation with higher energies resulting in deeper implanted NV centers. Subsequently, NV centers could be precharacterized and suitable single emitters chosen, featuring an ideal dipole orientation. Alternatively, also improved nanoimplantation techniques such as a maskless FIB-implantation of ions with high lateral resolution are in reach.<sup>86</sup> Eventually, the here generated NV centers feature an optical linewidth of several hundred gigahertz, whereas narrow line widths below 100 MHz are accessible,<sup>87</sup> at least in micrometer-thin RIE-etched diamond membranes. Smaller linewidths would further increase the total Purcell-factor. Therefore, in conclusion, higher SNR enhancements are within reach with the method presented here.

## ACKNOWLEDGMENTS

We thank B. Lagel and S. Wolff (Nano Structuring Center, University of Kaiserslautern) for helpful discussions on nanofabrication and use of their facilities. We further thank Alexander Huck and Simeon Bogdanov for helpful discussions on fluorescence contrast measurements and modeling. This research has been partially funded by the European Quantum Technology Flagship Horizon 2020 (No. H2020-EU1.2.3/2014-2020) under Grant No. 820394 (ASTERIQS). EU funding for the project AME-Lab (European Regional Development Fund Grant No. C/4-EFRE 13/2009/Br) for the FIB/SEM is acknowledged. E. Neu acknowledges funding via the NanoMatFutur program of the German Ministry of Education and Research (BMBF) under Grant No. FKZ13N13547 as well as a PostDoc Fellowship by the Daimler and Benz Foundation.

## REFERENCES

- M. W. Doherty, N. B. Manson, P. Delaney, F. Jelezko, J. Wrachtrup, and L. C. L. Hollenberg, "The nitrogen-vacancy colour centre in diamond," *Phys. Rep.* **528**, 1–45 (2013).
- M. W. Doherty, N. B. Manson, P. Delaney, and L. C. L. Hollenberg, "The negatively charged nitrogen-vacancy centre in diamond: The electronic solution," *New J. Phys.* **13**, 025019 (2011).
- N. Bar-Gill, L. Pham, A. Jarmola, D. Budker, and R. Walsworth, "Solid-state electronic spin coherence time approaching one second," *Nat. Commun.* **4**, 1743 (2013).
- M. H. Abobeih, J. Cramer, M. A. Bakker, N. Kalb, M. Markham, D. J. Twitchen, and T. H. Taminiau, "One-second coherence for a single electron spin coupled to a multi-qubit nuclear-spin environment," *Nat. Commun.* **9**, 2552 (2018).
- L. Robledo, L. Childress, H. Bernien, B. Hensen, P. Alkemade, and R. Hanson, "High-fidelity projective read-out of a solid-state spin quantum register," *Nature* **477**, 574–578 (2011).
- F. Jelezko, T. Gaebel, I. Popa, A. Gruber, and J. Wrachtrup, "Observation of coherent oscillations in a single electron spin," *Phys. Rev. Lett.* **92**, 076401 (2004).
- A. Gruber, A. Drabenstedt, C. Tietz, L. Fleury, J. Wrachtrup, and C. von Borczyskowski, "Scanning confocal optical microscopy and magnetic resonance on single defect centers," *Science* **276**, 2012–2014 (1997).

- <sup>8</sup>N. Kalb, P. C. Humphreys, J. J. Slim, and R. Hanson, "Dephasing mechanisms of diamond-based nuclear-spin memories for quantum networks," *Phys. Rev. A* **97**, 062330 (2018).
- <sup>9</sup>G. Thiering and A. Gali, "Theory of the optical spin-polarization loop of the nitrogen-vacancy center in diamond," *Phys. Rev. B* **98**, 085207 (2018).
- <sup>10</sup>P. Neumann, R. Kolesov, B. Naydenov, J. Beck, F. Rempp, M. Steiner, V. Jacques, G. Balasubramanian, M. L. Markham, D. J. Twitchen, S. Pezzagna, J. Meijer, J. Twamley, F. Jelezko, and J. Wrachtrup, "Quantum register based on coupled electron spins in a room-temperature solid," *Nat. Phys.* **6**, 249–253 (2010).
- <sup>11</sup>L. Robledo, H. Bernien, T. van der Sar, and R. Hanson, "Spin dynamics in the optical cycle of single nitrogen-vacancy centres in diamond," *New J. Phys.* **13**, 025013 (2011).
- <sup>12</sup>A. Dréau, M. Lesik, L. Rondin, P. Spinicelli, O. Arcizet, J.-F. Roch, and V. Jacques, "Avoiding power broadening in optically detected magnetic resonance of single NV defects for enhanced DC magnetic field sensitivity," *Phys. Rev. B* **84**, 195204 (2011).
- <sup>13</sup>M. Steiner, P. Neumann, J. Beck, F. Jelezko, and J. Wrachtrup, "Universal enhancement of the optical readout fidelity of single electron spins at nitrogen-vacancy centers in diamond," *Phys. Rev. B* **81**, 035205 (2010).
- <sup>14</sup>S. A. Wolf, I. Rosenberg, R. Rapaport, and N. Bar-Gill, "Purcell-enhanced optical spin readout of nitrogen-vacancy centers in diamond," *Phys. Rev. B* **92**, 235410 (2015).
- <sup>15</sup>J. G. Skellam, "The frequency distribution of the difference between two Poisson variates belonging to different populations," *J. R. Stat. Soc.* **109**, 296 (1946).
- <sup>16</sup>D. A. Hopper, R. R. Grote, S. M. Parks, and L. C. Bassett, "Amplified sensitivity of nitrogen-vacancy spins in nanodiamonds using all-optical charge readout," *ACS Nano* **12**, 4678–4686 (2018).
- <sup>17</sup>G. Kucsko, P. C. Maurer, N. Y. Yao, M. Kubo, H. J. Noh, P. K. Lo, H. Park, and M. D. Lukin, "Nanometre-scale thermometry in a living cell," *Nature* **500**, 54–58 (2013).
- <sup>18</sup>M. W. Doherty, V. V. Struzhkin, D. A. Simpson, L. P. McGuinness, Y. Meng, A. Stacey, T. J. Karle, R. J. Hemley, N. B. Manson, L. C. L. Hollenberg, and S. Praver, "Electronic properties and metrology applications of the diamond NV<sup>-</sup> center under pressure," *Phys. Rev. Lett.* **112**, 047601 (2014).
- <sup>19</sup>G. Balasubramanian, I. Y. Chan, R. Kolesov, M. Al-Hmoud, J. Tisler, C. Shin, C. Kim, A. Wojcik, P. R. Hemmer, A. Krüger, T. Hanke, A. Leitenstorfer, R. Bratschkitsch, F. Jelezko, and J. Wrachtrup, "Nanoscale imaging magnetometry with diamond spins under ambient conditions," *Nature* **455**, 648–651 (2008).
- <sup>20</sup>G. D. Fuchs, V. V. Dobrovitski, R. Hanson, A. Batra, C. D. Weis, T. Schenkel, and D. D. Awschalom, "Excited-state spectroscopy using single spin manipulation in diamond," *Phys. Rev. Lett.* **101**, 117601 (2008).
- <sup>21</sup>J. Maze, P. Stanwix, J. Hodges, S. Hong, J. Taylor, P. Cappellaro, L. Jiang, M. Dutt, E. Togan, A. Zibrov, A. Yacoby, R. Walsworth, and M. Lukin, "Nanoscale magnetic sensing with an individual electronic spin in diamond," *Nature* **455**, 644–647 (2008).
- <sup>22</sup>E. Bernardi, R. Nelz, S. Sonusen, and E. Neu, "Nanoscale sensing using point defects in single-crystal diamond: Recent progress on nitrogen vacancy center-based sensors," *Crystals* **7**, 124 (2017).
- <sup>23</sup>B. Hensen, H. Bernien, A. E. Dréau, A. Reiserer, N. Kalb, M. S. Blok, J. Ruitenberg, R. F. L. Vermeulen, R. N. Schouten, C. Abellán, W. Amaya, V. Pruneri, M. W. Mitchell, M. Markham, D. J. Twitchen, D. Elkouss, S. Wehner, T. H. Taminiau, and R. Hanson, "Loophole-free Bell inequality violation using electron spins separated by 1.3 kilometres," *Nature* **526**, 682–686 (2015).
- <sup>24</sup>P. Neumann, J. Beck, M. Steiner, F. Rempp, H. Fedder, P. R. Hemmer, J. Wrachtrup, and F. Jelezko, "Single-shot readout of a single nuclear spin," *Science* **329**, 542–544 (2010).
- <sup>25</sup>P. C. Maurer, G. Kucsko, C. Latta, L. Jiang, N. Y. Yao, S. D. Bennett, F. Pastawski, D. Hunger, N. Chisholm, M. Markham, D. J. Twitchen, J. I. Cirac, and M. D. Lukin, "Room-temperature quantum bit memory exceeding one second," *Science* **336**, 1283–1286 (2012).
- <sup>26</sup>A. Reiserer, N. Kalb, M. S. Blok, K. J. M. van Bemmelen, T. H. Taminiau, R. Hanson, D. J. Twitchen, and M. Markham, "Robust quantum-network memory using decoherence-protected subspaces of nuclear spins," *Phys. Rev. X* **6**, 021040 (2016).
- <sup>27</sup>S. Yang, Y. Wang, D. B. Rao, T. H. Tran, A. S. Momenzadeh, M. Markham, D. J. Twitchen, P. Wang, W. Yang, R. Stöhr, P. Neumann, H. Kosaka, and J. Wrachtrup, "High-fidelity transfer and storage of photon states in a single nuclear spin," *Nat. Photonics* **10**, 507–511 (2016).
- <sup>28</sup>K. Nemoto, M. Trupke, S. J. Devitt, B. Scharfenberger, K. Buczak, J. Schmiedmayer, and W. J. Munro, "Photonic quantum networks formed from NV centers," *Sci. Rep.* **6**, 26284 (2016).
- <sup>29</sup>F. Rozpedek, R. Yehia, K. Goodenough, M. Ruf, P. C. Humphreys, R. Hanson, S. Wehner, and D. Elkouss, "Near-term quantum-repeater experiments with nitrogen-vacancy centers: Overcoming the limitations of direct transmission," *Phys. Rev. A* **99**, 052330 (2019).
- <sup>30</sup>S. Wehner, D. Elkouss, and R. Hanson, "Quantum internet: A vision for the road ahead," *Science* **362**, eaam9288 (2018).
- <sup>31</sup>M. Jamali, I. Gerhardt, M. Rezai, K. Frenner, H. Fedder, and J. Wrachtrup, "Microscopic diamond solid-immersion-lenses fabricated around single defect centers by focused ion beam milling," *Rev. Sci. Instrum.* **85**, 123703 (2014).
- <sup>32</sup>J. P. Hadden, J. P. Harrison, A. C. Stanley-Clarke, L. Marseglia, Y.-L. D. Ho, B. R. Patton, J. L. O'Brien, and J. G. Rarity, "Strongly enhanced photon collection from diamond defect centers under microfabricated integrated solid immersion lenses," *Appl. Phys. Lett.* **97**, 241901 (2010).
- <sup>33</sup>P. Maletinsky, S. Hong, M. S. Grinolds, B. Hausmann, M. D. Lukin, R. L. Walsworth, M. Lončar, and A. Yacoby, "A robust scanning diamond sensor for nanoscale imaging with single nitrogen-vacancy centres," *Nat. Nanotechnol.* **7**, 320–324 (2012).
- <sup>34</sup>P. Appel, E. Neu, M. Ganzhorn, A. Barfuss, M. Batzer, M. Gratz, A. Tschöpe, and P. Maletinsky, "Fabrication of all diamond scanning probes for nanoscale magnetometry," *Rev. Sci. Instrum.* **87**, 063703 (2016).
- <sup>35</sup>T. M. Babinec, B. J. M. Hausmann, M. Khan, Y. Zhang, J. R. Maze, P. R. Hemmer, and M. Lončar, "A diamond nanowire single-photon source," *Nat. Nanotechnol.* **5**, 195–199 (2010).
- <sup>36</sup>B. J. M. Hausmann, B. Shields, Q. Quan, P. Maletinsky, M. McCutcheon, J. T. Choy, T. M. Babinec, A. Kubanek, A. Yacoby, M. D. Lukin, and M. Lončar, "Integrated diamond networks for quantum nanophotonics," *Nano Lett.* **12**, 1578–1582 (2012).
- <sup>37</sup>S. L. Mouradian, T. Schröder, C. B. Poitras, L. Li, J. Goldstein, E. H. Chen, M. Walsh, J. Cardenas, M. L. Markham, D. J. Twitchen, M. Lipson, and D. Englund, "Scalable integration of long-lived quantum memories into a photonic circuit," *Phys. Rev. X* **5**, 031009 (2015).
- <sup>38</sup>T.-Y. Huang, R. R. Grote, S. A. Mann, D. A. Hopper, A. L. Exarhos, G. G. Lopez, G. R. Kaighn, E. C. Garnett, and L. C. Bassett, "A monolithic immersion metalens for imaging solid-state quantum emitters," *Nat. Commun.* **10**, 2392 (2019).
- <sup>39</sup>A. Faraon, P. E. Barclay, C. Santori, K.-M. C. Fu, and R. G. Beausoleil, "Resonant enhancement of the zero-phonon emission from a colour centre in a diamond cavity," *Nat. Photonics* **5**, 301–305 (2011).
- <sup>40</sup>A. Faraon, C. Santori, Z. Huang, V. V. M. Acosta, and R. G. Beausoleil, "Coupling of nitrogen-vacancy centers to photonic crystal cavities in monocrystalline diamond," *Phys. Rev. Lett.* **109**, 033604 (2012).
- <sup>41</sup>B. J. M. Hausmann, B. J. Shields, Q. Quan, Y. Chu, N. P. de Leon, R. Evans, M. J. Burek, A. S. Zibrov, M. Markham, D. J. Twitchen, H. Park, M. D. Lukin, and M. Lončar, "Coupling of NV centers to photonic crystal nanobeams in diamond," *Nano Lett.* **13**, 5791–5796 (2013).
- <sup>42</sup>L. Li, T. Schröder, E. H. Chen, M. Walsh, I. Bayn, J. Goldstein, O. Gaathon, M. E. Trusheim, M. Lu, J. Mower, M. Cotlet, M. L. Markham, D. J. Twitchen, and D. Englund, "Coherent spin control of a nanocavity-enhanced qubit in diamond," *Nat. Commun.* **6**, 6173 (2015).
- <sup>43</sup>J. Riedrich-Möller, S. Pezzagna, J. Meijer, C. Pauly, F. Mücklich, M. Markham, A. M. Edmonds, and C. Becher, "Nanoimplantation and Purcell enhancement of single nitrogen-vacancy centers in photonic crystal cavities in diamond," *Appl. Phys. Lett.* **106**, 221103 (2015).
- <sup>44</sup>T. Schröder, M. Walsh, J. Zheng, S. Mouradian, L. Li, G. Malladi, H. Bakhrum, M. Lu, A. Stein, M. Heuck, and D. Englund, "Scalable fabrication of coupled NV center—Photonic crystal cavity systems by self-aligned N ion implantation," *Opt. Mater. Express* **7**, 1514–1524 (2017).
- <sup>45</sup>D. Riedel, I. Söllner, B. J. Shields, S. Starosielec, P. Appel, E. Neu, P. Maletinsky, and R. J. Warburton, "Deterministic enhancement of coherent photon generation

- from a nitrogen-vacancy center in ultrapure diamond," *Phys. Rev. X* **7**, 031040 (2017).
- <sup>46</sup>S. Bogdanović, S. B. van Dam, C. Bonato, L. C. Coenen, A.-M. J. Zwerver, B. Hensen, M. S. Z. Liddy, T. Fink, A. Reiserer, M. Lončar, and R. Hanson, "Design and low-temperature characterization of a tunable microcavity for diamond-based quantum networks," *Appl. Phys. Lett.* **110**, 171103 (2017).
- <sup>47</sup>J. T. Choy, B. J. M. Hausmann, T. M. Babinec, I. Bulu, M. Khan, P. Maletinsky, A. Yacoby, and M. Lončar, "Enhanced single-photon emission from a diamond-silver aperture," *Nat. Photonics* **5**, 738–743 (2011).
- <sup>48</sup>S. Bogdanov, M. Y. Shalaginov, A. Akimov, A. S. Lagutchev, P. Kapitanova, J. Liu, D. Woods, M. Ferrera, P. Belov, J. Irudayaraj, A. Boltasseva, and V. M. Shalaev, "Electron spin contrast of Purcell-enhanced nitrogen-vacancy ensembles in nanodiamonds," *Phys. Rev. B* **96**, 035146 (2017).
- <sup>49</sup>E. M. Purcell, "Spontaneous emission probabilities at radio frequencies," *Phys. Rev.* **69**, 681 (1946).
- <sup>50</sup>H. Bernien, L. Childress, L. Robledo, M. Markham, D. Twitchen, and R. Hanson, "Two-photon quantum interference from separate nitrogen vacancy centers in diamond," *Phys. Rev. Lett.* **108**, 043604 (2012).
- <sup>51</sup>A. Sipahigil, M. L. Goldman, E. Togan, Y. Chu, M. Markham, D. J. Twitchen, A. S. Zibrov, A. Kubanek, and M. D. Lukin, "Quantum interference of single photons from remote nitrogen-vacancy centers in diamond," *Phys. Rev. Lett.* **108**, 143601 (2012).
- <sup>52</sup>H. Bernien, B. Hensen, W. Pfaff, G. Koolstra, M. S. Blok, L. Robledo, T. H. Taminiau, M. Markham, D. J. Twitchen, L. Childress, and R. Hanson, "Heralded entanglement between solid-state qubits separated by three metres," *Nature* **497**, 86–90 (2013).
- <sup>53</sup>T. M. Babinec, H. Fedder, J. T. Choy, I. Bulu, M. W. Doherty, P. R. Hemmer, J. Wrachtrup, and M. Lončar, "Design of diamond photonic devices for spintronics," in *Conference on Lasers and Electro-Optics 2012* (Optical Society of America, 2012), Paper No. JW11.6.
- <sup>54</sup>S. B. van Dam, M. Ruf, and R. Hanson, "Optimal design of diamond-air microcavities for quantum networks using an analytical approach," *New J. Phys.* **20**, 115004 (2018).
- <sup>55</sup>T. Jung, L. Kreiner, C. Pauly, F. Mücklich, A. M. Edmonds, M. Markham, and C. Becher, "Reproducible fabrication and characterization of diamond membranes for photonic crystal cavities," *Phys. Status Solidi A* **213**, 3254–3264 (2016).
- <sup>56</sup>S. Pezzagna, D. Wildanger, P. Mazarov, A. D. Wieck, Y. Sarov, I. Rangeow, B. Naydenov, F. Jelezko, S. W. Hell, and J. Meijer, "Nanoscale engineering and optical addressing of single spins in diamond," *Small* **6**, 2117–2121 (2010).
- <sup>57</sup>Y. Tanaka, T. Asano, Y. Akahane, B. S. Song, and S. Noda, "Theoretical investigation of a two-dimensional photonic crystal slab with truncated cone air holes," *Appl. Phys. Lett.* **82**, 1661–1663 (2003).
- <sup>58</sup>E. Neu, P. Appel, M. Ganzhorn, J. Miguel-Sánchez, M. Lesik, V. Mille, V. Jacques, A. Tallaire, J. Achard, and P. Maletinsky, "Photonic nano-structures on (111)-oriented diamond," *Appl. Phys. Lett.* **104**, 153108 (2014).
- <sup>59</sup>P.-N. Volpe, P. Muret, F. Omnes, J. Achard, F. Silva, O. Brinza, and A. Gicquel, "Defect analysis and excitons diffusion in undoped homoepitaxial diamond films after polishing and oxygen plasma etching," *Diamond Relat. Mater.* **18**, 1205–1210 (2009).
- <sup>60</sup>J. Riedrich-Möller, E. Neu, and C. Becher, "Design of microcavities in diamond-based photonic crystals by Fourier- and real-space analysis of cavity fields," *Photonics Nanostruct.—Fundam. Appl.* **8**, 150–162 (2010).
- <sup>61</sup>L. Li, I. Bayn, M. Lu, C.-Y. Nam, T. Schröder, A. Stein, N. C. Harris, and D. Englund, "Nanofabrication on unconventional substrates using transferred hard masks," *Sci. Rep.* **5**, 7802 (2015).
- <sup>62</sup>D. M. Toyli, C. D. Weis, G. D. Fuchs, T. Schenkel, and D. D. Awschalom, "Chip-scale nanofabrication of single spins and spin arrays in diamond," *Nano Lett.* **10**, 3168–3172 (2010).
- <sup>63</sup>P. Spinicelli, A. Dréau, L. Rondin, F. Silva, J. Achard, S. Xavier, S. Bansropun, T. Debuisschert, S. Pezzagna, J. Meijer, V. Jacques, and J.-F. Roch, "Engineered arrays of nitrogen-vacancy color centers in diamond based on implantation of CN-molecules through nanoapertures," *New J. Phys.* **13**, 025014 (2011).
- <sup>64</sup>S. Pezzagna, D. Rogalla, H.-W. Becker, I. Jakobi, F. Dolde, B. Naydenov, J. Wrachtrup, F. Jelezko, C. Trautmann, and J. Meijer, "Creation of colour centres in diamond by collimated ion-implantation through nano-channels in mica," *Phys. Status Solidi A* **208**, 2017–2022 (2011).
- <sup>65</sup>I. Bayn, E. H. Chen, M. E. Trusheim, L. Li, T. Schröder, O. Gaathon, M. Lu, A. Stein, M. Liu, K. Kisslinger, H. Clevenson, and D. Englund, "Generation of ensembles of individually resolvable nitrogen vacancies using nanometer-scale apertures in ultrahigh-aspect ratio planar implantation masks," *Nano Lett.* **15**, 1751–1758 (2015).
- <sup>66</sup>M. Lesik, P. Spinicelli, S. Pezzagna, P. Happel, V. Jacques, O. Salord, B. Rasser, A. Delobbe, P. Sudraud, A. Tallaire, J. Meijer, and J.-F. Roch, "Maskless and targeted creation of arrays of colour centres in diamond using focused ion beam technology," *Phys. Status Solidi A* **210**, 2055–2059 (2013).
- <sup>67</sup>S. Pezzagna, D. Rogalla, D. Wildanger, J. Meijer, and A. Zaitsev, "Creation and nature of optical centres in diamond for single-photon emission—Overview and critical remarks," *New J. Phys.* **13**, 035024 (2011).
- <sup>68</sup>O. Lehtinen, B. Naydenov, P. Börner, K. Melentjevic, C. Müller, L. P. McGuinness, S. Pezzagna, J. Meijer, U. Kaiser, and F. Jelezko, "Molecular dynamics simulations of shallow nitrogen and silicon implantation into diamond," *Phys. Rev. B* **93**, 035202 (2016).
- <sup>69</sup>S. Pezzagna, B. Naydenov, F. Jelezko, J. Wrachtrup, and J. Meijer, "Creation efficiency of nitrogen-vacancy centres in diamond," *New J. Phys.* **12**, 065017 (2010).
- <sup>70</sup>K. Groot-Berning, N. Raatz, I. Dobrinets, M. Lesik, P. Spinicelli, A. Tallaire, J. Achard, V. Jacques, J.-F. Roch, A. M. Zaitsev, J. Meijer, and S. Pezzagna, "Passive charge state control of nitrogen-vacancy centres in diamond using phosphorous and boron doping," *Phys. Status Solidi A* **211**, 2268–2273 (2014).
- <sup>71</sup>K.-M. C. Fu, C. Santori, P. E. Barclay, and R. G. Beausoleil, "Conversion of neutral nitrogen-vacancy centers to negatively charged nitrogen-vacancy centers through selective oxidation," *Appl. Phys. Lett.* **96**, 121907 (2010).
- <sup>72</sup>L. Robledo, H. Bernien, I. van Weperen, and R. Hanson, "Control and coherence of the optical transition of single nitrogen vacancy centers in diamond," *Phys. Rev. Lett.* **105**, 177403 (2010).
- <sup>73</sup>J. Riedrich-Möller, L. Kipfstuhl, C. Hepp, E. Neu, C. Pauly, F. Mücklich, A. Baur, M. Wandt, S. Wolff, M. Fischer, S. Gsell, M. Schreck, and C. Becher, "One- and two-dimensional photonic crystal microcavities in single crystal diamond," *Nat. Nanotechnol.* **7**, 69–74 (2012).
- <sup>74</sup>J. C. Lee, D. O. Bracher, S. Cui, K. Ohno, C. A. McLellan, X. Zhang, P. Andrich, B. Aleman, K. J. Russell, A. P. Magyar, I. Aharonovich, A. B. Jayich, D. Awschalom, and E. L. Hu, "Deterministic coupling of delta-doped nitrogen vacancy centers to a nanobeam photonic crystal cavity," *Appl. Phys. Lett.* **105**, 261101 (2014).
- <sup>75</sup>S. Mosor, J. Hendrickson, B. C. Richards, J. Sweet, G. Khitrova, H. M. Gibbs, T. Yoshie, A. Scherer, O. B. Shchekin, and D. G. Deppe, "Scanning a photonic crystal slab nanocavity by condensation of xenon," *Appl. Phys. Lett.* **87**, 141105 (2005).
- <sup>76</sup>J. Preclíková, F. Trojánek, B. Dzurňák, P. Malý, A. Kromka, and B. Rezek, "Light-assisted adsorption processes in nanocrystalline diamond membranes studied by femtosecond laser spectroscopy," *Diamond Relat. Mater.* **19**, 918–922 (2010).
- <sup>77</sup>R. Albrecht, A. Bommer, C. Deutsch, J. Reichel, and C. Becher, "Coupling of a single nitrogen-vacancy center in diamond to a fiber-based microcavity," *Phys. Rev. Lett.* **110**, 243602 (2013).
- <sup>78</sup>P. Appel, M. Ganzhorn, E. Neu, and P. Maletinsky, "Nanoscale microwave imaging with a single electron spin in diamond," *New J. Phys.* **17**, 112001 (2015).
- <sup>79</sup>L. Rondin, J.-P. Tetienne, T. Hingant, J.-F. Roch, P. Maletinsky, and V. Jacques, "Magnetometry with nitrogen-vacancy defects in diamond," *Rep. Prog. Phys.* **77**, 056503 (2014).
- <sup>80</sup>M. Chipaux, A. Tallaire, J. Achard, S. Pezzagna, J. Meijer, V. Jacques, J.-F. Roch, and T. Debuisschert, "Magnetic imaging with an ensemble of nitrogen-vacancy centers in diamond," *Eur. Phys. J. D* **69**, 166 (2015).
- <sup>81</sup>B. K. Ofori-Okai, S. Pezzagna, K. Chang, M. Loretz, R. Schirhagl, Y. Tao, B. A. Moores, K. Groot-Berning, J. Meijer, and C. L. Degen, "Spin properties of very shallow nitrogen vacancy defects in diamond," *Phys. Rev. B* **86**, 081406 (2012).
- <sup>82</sup>N. B. Manson, J. P. Harrison, and M. J. Sellars, "Nitrogen-vacancy center in diamond: Model of the electronic structure and associated dynamics," *Phys. Rev. B* **74**, 104303 (2006).

- <sup>83</sup>M. L. Goldman, A. Sipahigil, M. W. Doherty, N. Y. Yao, S. D. Bennett, M. Markham, D. J. Twitchen, N. B. Manson, A. Kubanek, and M. D. Lukin, "Phonon-induced population dynamics and intersystem crossing in nitrogen-vacancy centers," *Phys. Rev. Lett.* **114**, 145502 (2015).
- <sup>84</sup>A. Young, C. Y. Hu, L. Marseglia, J. P. Harrison, J. L. O'Brien, and J. G. Rarity, "Cavity enhanced spin measurement of the ground state spin of an NV center in diamond," *New J. Phys.* **11**, 013007 (2009).
- <sup>85</sup>J.-P. Tetienne, L. Rondin, P. Spinicelli, M. Chipaux, T. Debuisschert, J.-F. Roch, and V. Jacques, "Magnetic-field-dependent photodynamics of single NV defects in diamond: An application to qualitative all-optical magnetic imaging," *New J. Phys.* **14**, 103033 (2012).
- <sup>86</sup>T. Schröder, M. E. Trusheim, M. Walsh, L. Li, J. Zheng, M. Schukraft, A. Sipahigil, R. E. Evans, D. D. Sukachev, C. T. Nguyen, J. L. Pacheco, R. M. Camacho, E. S. Bielejec, M. D. Lukin, and D. Englund, "Scalable focused ion beam creation of nearly lifetime-limited single quantum emitters in diamond nanostructures," *Nat. Commun.* **8**, 15376 (2017).
- <sup>87</sup>M. Ruf, M. Ijspeert, S. van Dam, N. de Jong, H. van den Berg, G. Evers, and R. Hanson, "Optically coherent nitrogen-vacancy centers in micrometer-thin etched diamond membranes," *Nano Lett.* **19**, 3987–3992 (2019).